Supplementary Material for "Mapping Population-based Structural Connectomes"

Zhengwu Zhang[a,b], Maxime Descoteaux[c], Jingwen Zhang[d], Gabriel Girard[c], Maxime Chamberland[c], David Dunson[a], Anuj Srivastava[e], Hongtu Zhu[f,d]

[a]*Department of Statistical Science, Duke University, Durham, USA*
[b]*Statistical and Applied Mathematical Sciences Institute, Durham, USA*
[c]*Computer Science Department, Faculty of Science, University of Sherbrooke, Sherbrooke, QC, Canada*
[d]*Department of Biostatistics, University of North Carolina at Chapel Hill, Chapel Hill, NC, USA*
[e]*Department of Statistics, Florida State University, Tallahassee, FL, USA*
[f]*Department of Biostatistics, University of Texas MD Anderson Cancer Center, Houston, TX, USA*

1. Gray Matter Dilation

Figure 1 illustrates the effect of the dilation procedure in PSC pipeline. PSC contains an iterative dilation procedure, i.e. each time, we dilate the current gray matter (GM) ROIs to white matter (WM) region by 1 voxel; if there are ψ ($\psi > 1$) voxels to dilate, we perform such dilation iteratively ψ times. The procedure for dilating 1 voxel is given in Algorithm 1.

2. Calculation of Connected Surface Area (CSA) Feature

From the definition of the CSA feature, we can easily identify that it contains an area measure. In order to calculate the CSA, we need to identify the surface of an ROI and the intersections of the surface and streamlines. The ROI is composed of a set of 3D voxels. In our implementation, for simplicity, the total surface area of such ROI is approximated by the number of voxels in the boundary of this ROI. Figure 2 (a) illustrates a 2D ROI example, and

Algorithm 1: Dilation of one voxel from GM ROI to WM regions

Input: One parcellation containing GM ROI and WM labels.

1. Identify all the white matter voxels in this parcellation.
2. For each white matter voxel, treat it as a center and draw a square window (with size $5 \times 5 \times 5$) to extract its neighborhood label information.
   (a) Analyze the label information in the window to cluster the center white matter voxel.
   (b) If there is no gray matter label in the neighborhood, return the original white matter label.
   (c) If there are one or more gray matter labels. Sort the gray matter labels based on its occurence. From the most frequent one, calculate the distances of these gray matter voxels to current center white matter voxel, if the minimal distance is smaller than $\sqrt{3}$, assign the white matter voxel to this gray matter one. Otherwise, continue for the next frequent gray matter voxel. If none of the minimal distance is smaller than $\sqrt{3}$, return the original white matter label.
3. Assign the centered white matter voxel with the returned label.

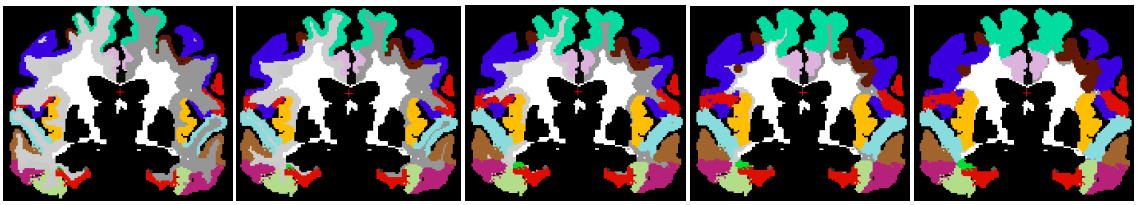

Figure 1: Illustration of gray matter dilation.

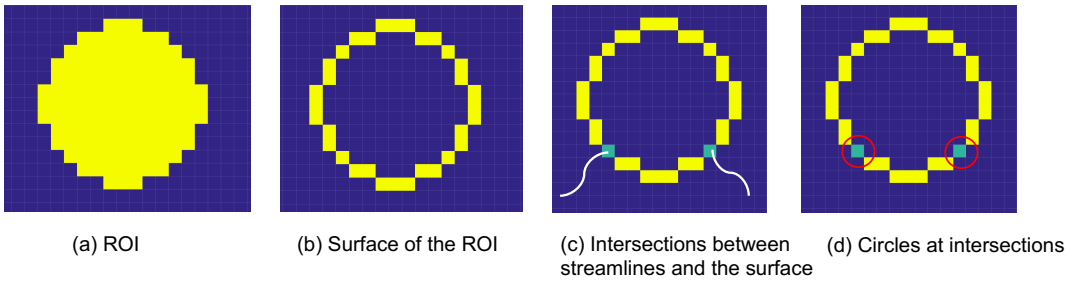

Figure 2: Illustration of calculating the CSA for a given ROI.

its area is approximated by the number of voxels in the boundary in (b) (the approximation precision is related to the size of the voxel). For a fixed circle size, i.e. radius r fixed, Algorithm 2 describes how to calculate the CSA feature.

Algorithm 2: Extraction of CSA feature

Input: Two ROIs V_1 and V_2, the streamlines connecting these two ROIs, and the circle radius r. Each ROI contains a set of voxels, $V_i = \{v_1, ..., v_{n_i}\}$ for $i = 1, 2$, where each v_j is a voxel in 3D space.

1. Identify the voxels in the contours of two ROIs V_1 and V_2 (illustrated in Figure 2 (b)), denoted as BV_1 and BV_2. For each ROI, identify the subset of voxels that intersect with the streamlines connecting two ROIs on the surface (illustrate in Figure 2 (c)). Denote the voxels at the intersection as IV_1 and IV_2.
2. At each intersection voxel $v_j \in IV_i$ for $i = 1, 2$, draw a sphere with a fixed radius r and with its center overlapped with the center of v_j. Record the voxels within this sphere in the set of $SphV_{v_j}$
3. The union of $\cup_{v_j} SphV_{v_j}$ for $v_j \in IV_1 \cup IV_2$ contains all voxels of the proposed CSA feature. The number of voxels (or the volume) in $\cup_{v_j} SphV_{v_j}$ is deemed as our CSA feature.

3. Different Distance Metrics for Comparing Weighted Networks.

In the main paper, we only use the $\mathbb{L}^2$ metric to calculate dICC scores for various weighted networks extracted from the PSC framework. Here, we are interested in exploring the reproducibility scores under the combination of different metrics and transformations of weighted networks. The goal is to identify the combination of metric and transformation that has the best reproducibility for weighted network analysis. The following distances are used:

$$d_{w1} = \|A_1 - A_2\|, \qquad d_{w2} = \|\widehat{A}_1 - \widehat{A}_2\|,$$
$$d_{w3} = |A_1 - A_2|, \qquad d_{w4} = |\widehat{A}_1 - \widehat{A}_2|,$$

where $\|\cdot\|$ is the $\mathbb{L}^2$ metric, $|\cdot|$ is the $\mathcal{L}^1$ metric, and $\widehat{A}$ is the logarithm transform of A such that $\widehat{A}(a,b) = \log(A(a,b)+1)$. Table 1 presents the result of dICC calculated using different distances with the test-retest dataset. By comparing the different distances, we find that d_{w1} almost always has the highest dICC score. Therefore, to achieve the best discriminative power, we recommend to use the raw weighted matrix with the $\mathbb{L}^2$ metric for weighted network analysis.

4. More Results for the Compression Procedure

4.1. Simulation study for representation efficiency of PTCS

In this section, we perform a simulation study to illustrate the representation efficiency of the proposed parcellation-based tractography common space (PTCS) algorithm.

We want to illustrate how the variation decomposition (alignment) process and functional principal component analysis (FPCA) can efficiently represent all streamlines connecting a pair of brain regions. We first simulated

Table 1: Comparison of reproducibility (dICC score) of different distances. The highest dICC score calculated under each distance is bold.

Features	$V = 68$				$V = 148$			
	d_{w1}	d_{w2}	d_{w3}	d_{w4}	d_{w1}	d_{w2}	d_{w3}	d_{w4}
PSC Mean FA	.462	.450	.442	.435	.577	.574	.421	.417
PSC Max FA	.389	.394	.387	.390	.541	.546	.378	.382
PSC Cluster #	.798	.711	.573	.480	.755	**.690**	.490	.438
PSC Ave. Len.	.519	.477	.563	.560	.539	.542	.443	.441
PSC Count	.791	.712	.700	.551	.731	.677	.649	.515
PSC CSA	**.808**	.670	**.715**	.534	**.762**	.678	**.668**	.500
PSC wCSA	.751	**.750**	.669	**.667**	.666	.663	.607	**.605**
General Count	.403	.695	.578	.588	.545	.669	.578	.531
General Binary	-	-	.434	-	-	-	.426	-

200 streamlines with similar shapes, but random lengths, translations, rotations and re-parameterizations. To be more specific, we extracted 200 streamlines connecting left occipital and right occipital (they have similar shapes). The 200 streamlines were then aligned by removing the scaling, translation, roation and re-parameterization. Next, 200 randomly generated scalings, translations, rotations and re-parameterizations were applied to these streamlines. Figure 3 shows these simulated curves.

The simulated streamlines were then aligned by separating different shape confounding parameters, including (1) translations only, (2) rotations and translations, and (3) separating rotations, translations and re-parameterizations. Fig. 4 shows the alignment results under the three scenarios. It indicates that by separating more shape confounding variables from the shape component, it leads to tighter residual shape information, and therefore reduces the number of basis functions needed to represent each streamline. Under each scenario, we performed fPCA, learned a set of basis functions from the aligned streamlines, and represented all streamlines by using the learnt basis func-

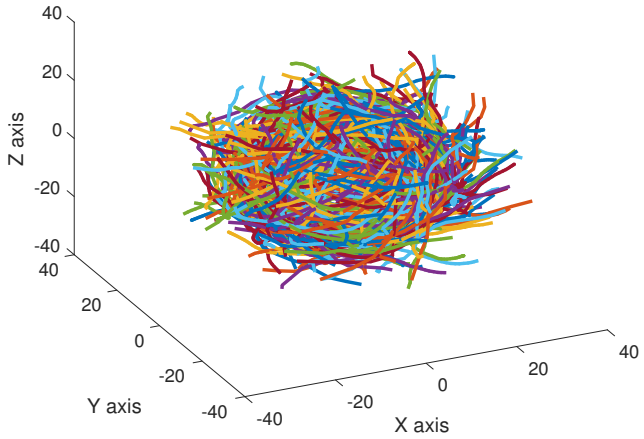

Figure 3: The 200 simulated streamlines.

tions. Let f_i be the raw streamlines and $\widehat{f}_{i,M}$ be the reconstructed streamlines obtained by using the first M number of fPCA basis functions for each coordinate. We measure the difference between f_i and $\widehat{f}_{i,M}$ by using the integrated squared error (ISE) defined as $\text{ISE}_i(M) = \sqrt{\int_0^1 |\widehat{f}_{i,M}(s) - f(s)|^2 ds}$. As expected, increasing M and separating more shape confounding variables reduces $\text{ISE}_i(M)$. See the right panel of Fig. 4 for details. Under scenario (3), we do not need the re-parameterization in order to recover the original streamline path. Another issue with scenario (3) is that, under a naive implementation, it is time consuming to separate the re-parameterization (Srivastava et al., 2011). To speed up the alignment process, we can either use a fast approximate alignment procedure (Huang et al., 2016) under scenario (3) or only separate out rotation and translation under scenario (2).

4.2. Robustness of the PTCS

To future test the robustness of the learnt PTCS from HCP subjects, we run our PSC pipeline in three other datasets with relatively low image

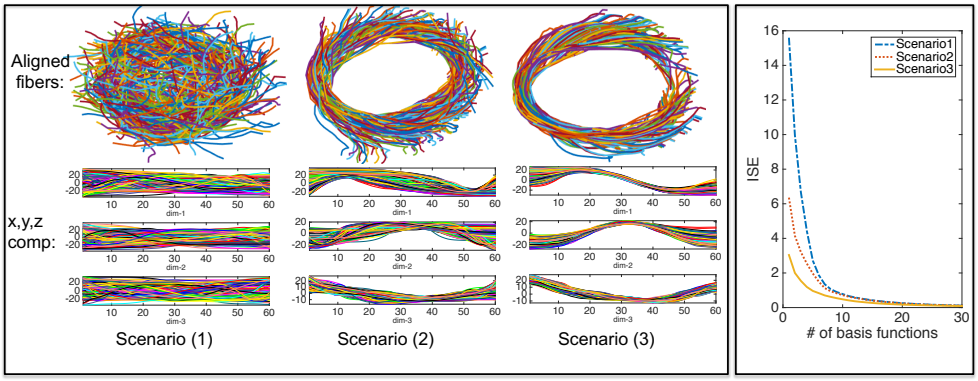

Figure 4: Comparison of the representation efficiency at different scenarios of separating shape confounding parameters.

quality. To be specific, we used 20 HCP subjects a the training data, and learnt a template fiber and set of basis functions to compress the streamlines. For the connivence of compression, here we used the three connections (L28,R28), (L3, R28), (LS9, R23) (based on the Desikan-Killiany parcellation) as presented in the main paper.

Three subjects from three different datasets were used.

1. Sherbrooke Test-Retest Dataset: As presented in the main paper, DTI image in this dataset was acquired along 64 uniformly distributed directions with a b-value of $b = 1000\ s/mm^2$ and a single b_0 (=0 s/mm^2) image. Scans were done by using the single-shot echo-planar imaging sequence on a 1.5 Tesla Siemens MAGNETOM (128×128 matrix, 2 mm isotropic resolution, TR/TE 11000/98 ms and GRAPPA factor 2).
2. Philadelphia Neurodevelopmental Cohort (PNC) Dataset: The diffusion space (q-space) was acquired along 32 uniformly distributed directions with a b-value of $b = 1000\ s/mm^2$ and 4 b_0 (=0 s/mm^2) images (Satterthwaite et al., 2016). Scans were done by using a single

3T Siemens TIM Trio whole-body scanner using the VB17 revision of the Siemens software. Each DTI image has the isotropic resolution of $1.875 \times 1.875 \times 2\ mm^3$. Signal excitation and reception were obtained using a quadrature body coil for transmit and a 32-channel head coil for receive.

3. High Resolution DTI: DTI image in this dataset has a high SNR and sub-millimeter isotropic resolution (specifically: $0.85 \times 0.85 \times 0.85\ mm^3$) (Chang et al., 2015). Images was scanned from a 3 Tesla clinical MRI scanner (MR750, General Electric, Waukesha, WI, USA), equipped with an 8-channel head coil. The diffusion space (q-space) was acquired along 12 uniformly distributed directions with a b-value of $b = 800\ s/mm^2$ and 1 b_0 ($=0\ s/mm^2$) image.

All images from these datasets were processed using our PSC framework. Streamlines of each subject were extracted and saved for compression. Table 3 (in this letter) shows the compression result. The results for the Sherbrooke Test-Restest and the PNC datasets are based $n = 5$ subjects, and the results for high resolution DTI dataset are based on only 1 subject since we only obtained one from our collaborators now. Table 3 shows the compression result. Compared with the HCP data, we observe a slightly decreasing of the compression power (which is normal because the PTCS is learned based on the HCP datasets). Tractography data constructed from the PNC subjects have the worst quality because of the image resolution (spatial resolution and q-space resolution). However, using the basis functions learned from the HCP dataset, our compression method still can achieve good compression rates. Figure 5 shows tracts before and after compression from one PNC subject.

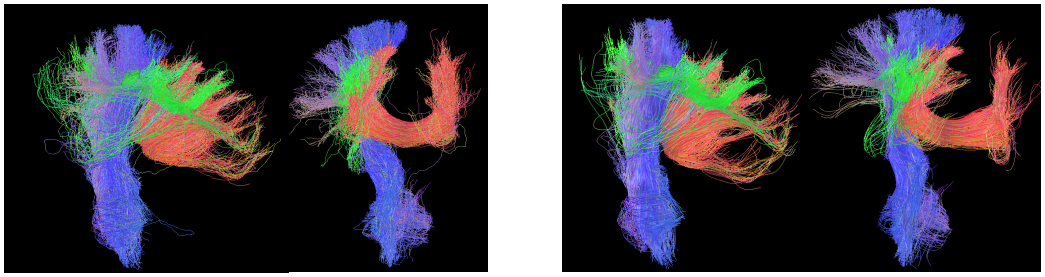

Figure 5: Evaluation of the proposed compression method with one PNC subject. The basis functions were learned using the HCP subjects. Here we directly applied the learned basis to represent the streamlines extracted from one PNC subject. Similar compression power is observed comparing with the HCP result.

Table 2: Compression ratios (in percentage) of tractography generated from data in three different sites. Standard deviation is shown in the subscript parenthesis.

	Connection $(LS9, R23)$				Connection $(L3, R28)$				Connection $(L28, R28)$			
$\|\epsilon\|$ (mm)	0.1	0.2	0.5	2.0	0.1	0.2	0.5	2.0	0.1	0.2	0.5	2.0
Sherbrooke (n=5)	$95.6_{(.2)}$	$97.3_{(.1)}$	$98.6_{(.1)}$	$99.1_{(.1)}$	$95.5_{(.1)}$	$97.2_{(.1)}$	$98.4_{(.1)}$	$98.9_{.0}$	$95.8_{(.1)}$	$97.6_{(.0)}$	$98.7_{(.1)}$	$99.2_{(.0)}$
PNC (n=5)	$95.2_{(.1)}$	$97.2_{(.1)}$	$98.5_{(.1)}$	$99.1_{(.1)}$	$95.2_{(.2)}$	$97.1_{(.1)}$	$98.3_{(.1)}$	$98.8_{(.1)}$	$95.2_{.1}$	$97.3_{(.1)}$	$98.6_{.1}$	$99.2_{.0}$
High Res (n=1)	95.5	97.3	98.6	99.1	96.6	97.8	98.8	99.3	95.1	97.4	98.6	99.2

Table 3: Mean diffusion integrity changes (%) after compression in each connection

	$(LS9, R23)$				$(L3, R28)$				$(L28, R28)$			
$\|\epsilon\|$ (mm)	0.1	0.2	0.5	2.0	0.1	0.2	0.5	2.0	0.1	0.2	0.5	2.0
FA	.03	.06	.46	6.1	.05	.15	.50	2.5	.05	.08	0.38	5.1
MD	.01	.02	.10	2.3	.01	.02	.07	.64	.01	.06	.58	2.9

4.3. Impact of Diffusion Measures Along Bundles After Compression

In this section, we are interested in studying the impact of the compression of streamlines to the diffusion measures along them. Taking FA and MD measures as one example, we performed additional experiments to explore how the new representation of streamlines can impact the integrity of diffusivity information along fiber bundles that connect any two regions. Table 3 shows the percentage of mean FA and MD changes after compressing along the three selected connections shown in Figure 9 in the main paper. The percentage is calculated based $100 * |v_{bf} - v_{af}|/v_{bf}$, where v_{bf} represents the value before compressing and v_{af} represents the value after compressing.

5. Heritability of Weighted Structural Network

In Table 4, we show more details about the selected 28 significant connections with heritability scores greater than 0.8, the heritability score h^2, the ROI names and the adjusted p-values. This analysis used mean FA weight matrix (under the Desikan-Killiany parcellation) as the phenotype of interest.

Table 4: Selected connections with heritability larger than 0.8. The p-values are adjusted by Bonferroni correction. h^2 is referred as the heritability score. This analysis used mean FA weight matrix (under the Desikan-Killiany parcellation) as the phenotype of interest.

ROI1	ROI2	h^2	p-value
L10 (lh-lateraloccipital)	R20 (rh-pericalcarine)	0.976	<6.27E-14
L28 (lh-superiorparietal)	R4 (rh-cuneus)	0.971	<6.27E-14
L34 (lh-insula)	R28 (rh-superiorparietal)	0.966	<6.27E-14
L34 (lh-insula)	R9 (rh-isthmuscingulate)	0.959	<6.27E-14
L20 (lh-pericalcarine)	R28 (rh-superiorparietal)	0.954	<6.27E-14
L24 (lh-precuneus)	R4 (rh-cuneus)	0.954	<6.27E-14
L28 (lh-superiorparietal)	R10 (rh-lateraloccipital)	0.952	<6.27E-14
L31 (lh-frontalpole)	R31 (rh-frontalpole)	0.952	<6.27E-14
L3 (lh-caudalmiddlefrontal)	R3 (rh-caudalmiddlefrontal)	0.95	<6.27E-14
L7 (lh-inferiorparietal)	R28 (rh-superiorparietal)	0.944	<6.27E-14
L20 (lh-pericalcarine)	R20 (rh-pericalcarine)	0.944	<6.27E-14
L28 (lh-superiorparietal)	R20 (rh-pericalcarine)	0.937	<6.27E-14
L16 (lh-paracentral)	R23 (rh-precentral)	0.928	<6.27E-14
L7 (lh-inferiorparietal)	R24 (rh-precuneus)	0.918	1.39E-13
R8 (rh-inferiortemporal)	R11 (rh-lateralorbitofrontal)	0.906	7.65E-13
L31 (lh-frontalpole)	R27 (rh-superiorfrontal)	0.904	2.09E-13
L9 (lh-isthcingulate)	R28 (rh-superiorparietal)	0.902	2.16E-12
L7 (lh-inferiorparietal)	L24 (lh-precuneus)	0.901	1.87E-10
L10 (lh-lateraloccipital)	R9 (rh-isthcingulate)	0.884	1.29E-10
R14 (rh-middletemporal)	R26 (rh-rostmidfrontal)	0.876	2.01E-10
L1 (lh-bankssts)	L17 (lh-parsopercularis)	0.874	1.55E-09
L34 (lh-insula)	R27 (rh-superiorfrontal)	0.873	2.07E-09
L4 (lh-cuneus)	R20 (rh-pericalcarine(54)	0.866	3.44E-08
L15 (lh-parahippocampal)	L20 (lh-pericalcarine)	0.856	7.59E-08
L10 (lh-lateraloccipital)	L34 (lh-insula)	0.827	8.34E-07
L24 (L-precuneus)	L29 (lh-superiortemporal)	0.811	4.83E-07
L11 (lh-lateralorbitofrontal)	L17 (lh-parsopercularis)	0.811	4.19E-06
L28 (lh-superiorparietal)	R28 (rh-superiorparietal)	0.804	5.99E-06

Chang, H.C., Sundman, M., Petit, L., Guhaniyogi, S., Chu, M.L., Petty, C., Song, A.W., Chen, N.k., 2015. Human brain diffusion tensor imaging at submillimeter isotropic resolution on a 3tesla clinical mri scanner. NeuroImage 118, 667–675.

Huang, W., Gallivan, K.A., Srivastava, A., Absil, P.A., 2016. Riemannian optimization for registration of curves in elastic shape analysis. Journal of Mathematical Imaging and Vision 54, 320–343.

Satterthwaite, T.D., Connolly, J.J., Ruparel, K., Calkins, M.E., Jackson, C., Elliott, M.A., Roalf, D.R., Hopson, R., Prabhakaran, K., Behr, M., et al., 2016. The philadelphia neurodevelopmental cohort: a publicly available resource for the study of normal and abnormal brain development in youth. Neuroimage 124, 1115–1119.

Srivastava, A., Klassen, E., Joshi, S., Jermyn, I., 2011. Shape analysis of elastic curves in Euclidean spaces. IEEE Trans. Pattern Anal. Mach. Intell. 33, 1415–1428.